Available online at www.sciencedirect.com

Manufacturing Letters

Manufacturing Letters 41 (2024) 1046–1054

52nd SME North American Manufacturing Research Conference (NAMRC 52, 2024)

Towards Gradient Design of TPMS lattices and Laser Powder Bed Fusion Processing– Role of Laser Strategies and Lattice Thickness

Avez Shaikh[a], Jacklyn Griffis[a], Ryan Stebbins[a], Kazi Safowan Shahed[b], Ankit Saxena[a], Andrew Ross[c], Guha Manogharan [a,b*]

[a] *Department of Mechanical Engineering Pennsylvania State University, University Park PA – 16803, USA.*
[b] *Department of Industrial and Manufacturing Engineering Pennsylvania State University, University Park PA – 16803, USA.*
[c] *Center of Quantitative Imaging, Institute of Energy and the Environment, Pennsylvania State University, , University Park PA – 16803, USA.*
* Corresponding author. *E-mail address:* gum53@psu.edu

Abstract

The ability to manufacture complex design geometries via Additive Manufacturing (AM) has led to a rapid growth in advancing the design methods, fabrication, and application of Triply Periodic Minimal Surface (TPMS) lattices with minimal surface topologies. Due to its zero-mean curvature, TPMS lattices can be additively manufactured without any sacrificial support structures and offer both design and manufacturing engineers, unprecedented control over the local physical properties (surface area, relative density, etc.) and local mechanical properties (flexural strength, Young's modulus, etc.). TPMS lattices are of high interest for a wide range of applications such as biomedical implants, energy absorption, and surface fluidic applications such as heat exchangers, and energy storage. Recent advancements in functionally graded TPMS lattice design by varying local lattice geometry has shown to result in different mechanical performance. However, there have been limited studies in understanding the functional grading of AM process conditions (e.g., Laser-Powder Bed Fusion in this study) and lattice sheet thickness to better map the design-processing conditions-properties. The goal of this study is to achieve similar mechanical properties in TPMS sheet lattices with two different TPMS sheet thicknesses by varying laser processing conditions (e.g., contour and hatch conditions in this study). Quasi-static tensile testing of solid samples with corresponding AM conditions and 3-point bending tests of TPMS lattices were performed in accordance with ASTM E8 and ASTM E290, respectively. It was observed that the flexural properties of the 0.75mm and 0.25 mm TPMS lattices are similar and exhibit different properties with different scan strategies and speed variations under contour-only and hatch-only laser scanning strategies. Also, the 0.75 mm TPMS sheet lattices exhibited 79% higher flexural stiffness than the 0.25mm sheet lattices. It was also observed that this observed trend was reversed in the case of tensile properties. Findings from this study can provide new directions towards achieving gradient TPMS lattice designs with varying local mechanical performance by grading the laser scanning strategies to achieve desired mechanical properties and surface topologies.

Peer-review under responsibility of the scientific committee of the NAMRI/SME.
Keywords: TPMS; LPBF; gradient design, mechanical properties,

1. Introduction

Triply Periodic minimal surfaces (TPMS) are mathematically defined non–intersecting surfaces that divide 3-dimensional space into multiple repeatable and non-intersecting domains that are self-supporting, i.e. do not require sacrificial support during additive manufacturing (AM) processing, [1]. The diamond and gyroid TPMS are the most well-known surfaces and have been extensively investigated for topology-driven material development [2]. TPMS cellular materials hold multiple advantages over conventional strut and plate-based cellular architecture. Their robust mathematical design structure and ease of functional grading allow for the rapid implementation of topology-driven models for achieving unique mechanical properties such high strength-to-weight ratio, high energy absorption, high surface-to-volume ratio, and high thermal conduction [3]. The smooth topology of TPMS surfaces lacks sharp edges and stress concentration points and

Peer-review under responsibility of the scientific committee of the NAMRI/SME.

the stretching-dominated architecture of TPMS lattices provides superior mechanical performance compared to lattices with bending architecture. Micro-scale topological imperfections caused during manufacturing can have a significant effect on macro-scale mechanical properties [4]. TPMS surface topologies have a significant advantage over conventional plat-strut type lattices owing to their zero mean curvature and large surface areas. [5,6]

TPMS based lattices have been implemented in a wide range of applications involving fluid structure interactions, batteries, catalytic converters, and fuel cells owing to their high surface are to volume ratio [7]. Ouda et al., (2020) [8] redesigned feed spacers using TPMS structures for direct contact membrane distillation and reverse osmosis. TPMS based feed spaces were found to be more effective at reducing fouling and enhancing turbulence than their commercially available counterparts. Elliot et al (2017) [9] investigated the topologies of biofilter media carriers that determine the performance of moving bed biofilm reactors used for wastewater treatment. Media carriers redesigned with sheet network and gyroid topologies had comparable rates of ammonia removal to that of commercially available media. Al-Ketan et al (2019) [10] fabricated and tested TPMS based ceramic catalytic substrates based on solid-network and sheet network designs. TPMS based substrates showed a reduced pressure drop with higher compressive strength and the highest in gyroid sheet network substrates. Werner et al (2015) [11] created Lithium-ion/sulphur energy storage system with an ultrathin 3D gyroidal electrolyte phase. A stable open-circuit voltage was observed in their electrochemical analysis demonstrating battery like functionality with a significantly smaller footprint than similar 2D thin layer design. TPMS based heat exchangers designed by Femmer et al (2015) [12] have better performance when compared to flat sheet heat exchangers. TPMS based reinforcements have also been used to enhance the mechanical properties of interpenetrating phase composites (IPC). Biomedical applications such as tissue engineering have also benefitted from the mathematically driven topological attributes of TPMS structures. [13] Rajagopalan et al, (2006) [14] presented an early study on TPMS based scaffolds for tissue regeneration. The influence of scaffold architecture on tissue regeneration parameters such has cell seeding and settling speeds have been studied extensively by previous investigators.

Additive manufacturing has played a significant role in the fabrication of lattices with TPMS topologies. Due to their self-supporting nature [26], TPMS lattices can be additively manufactured with high dimensional accuracy using different AM processing methods such as Stereolithography ([15],[16], [17],[18]) Laser Powder Bed Fusion ([19],[21],[22]) and material jetting ([23],[24],[25]) at a wide range of materials such as titanium, stainless steel, polymers and ceramics. Depending on the AM process, TPMS-enabled smooth curved surfaces facilitate post-processing procedures such as powder and resin removal. To the best of the authors' knowledge, there are limited studies on the exploration of processing conditions (e.g., laser power, scan speed, and scanning strategy) on the resulting microstructure, AM process induced defects and ultimately, mechanical properties of TPMS lattice-structured metal parts, especially Ti6Al4V produced by LPBF. Qu et al. (2021) [34] explored optimal process parameters for micro-scale LPBF of SS316L, determining them through cubes and thin-walled TPMS gyroid structures of different sheet thickness. They achieved a component density of 99.7% with an energy density of 100 J/mm³ using specific parameters, and identified a parameter set resulting in 100μm thin and continuous walls with superior dimensional accuracy. Hussain et al. (2024) [35] conducted a comprehensive study investigating the phase transformation behaviour of NiTi shape memory alloy (SMA) TPMS lattices fabricated via LPBF. Their findings emphasize the importance of considering the interplay between structural geometry, material properties, and process parameters in the design of SMA structures. Specifically, they observed significant effects of scanning speed and laser power on the thermal behaviour of both primitive and gyroid TPMS samples.

In this paper, the effects of laser processing conditions on the mechanical properties of TPMS surface lattices are systematically investigated. The goal of this study is to achieve similar mechanical properties with 2 different TPMS sheet thicknesses. The motivation for this study is to enable the design and manufacturing of gradient thickness lattice structures with similar mechanical properties and functionally graded density. Such locally engineered properties are highly desirable for applications such as robotics, fracture-fixation implants, and light-weight structures. To this end, TPMS lattices with two sheet thicknesses were characterized using mechanical testing (3-point bending test). Mechanical test coupons were manufactured using LPBF. Micro-CT was used to better understand the as-built component densities of the samples manufactured.

2. Methodology

2.1. Design and Manufacturing

The TPMS gyroid topology was modeled in nTopology (version: 4.9.3, New York, USA), using two different sheet thickness 0.25mm and 0.75mm, respectively. The designed relative densities (ρ*) of 0.25mm and 0.75mm sheet thicknesses are 0.048 and 0.145 and is calculated using ($\rho_{lattice}/\rho_{solid}$) [34]. Using the process parameters detailed in Table 1, 3DXpert (version 2022, 3D Systems, Inc., USA) was used to generate the build plan (Figure 1) for the fabrication of the study specimens using nominal parameters in the ProX DMP 320 (3D Systems, Inc., USA) L-PBF machine produce each sample. Six distinct process variations were implemented, each employing one of two different scan strategies (Figure 2) to induce different processing conditions (i.e., scan speed and scan pattern) (Table 1). For each strategy, the scan speed was adjusted from its nominal speed, with variations involving both a 15% increase and a 15% decrease. A control sample was also manufactured with the default machine specified nominal process parameters (Table 2). The feedstock material utilized

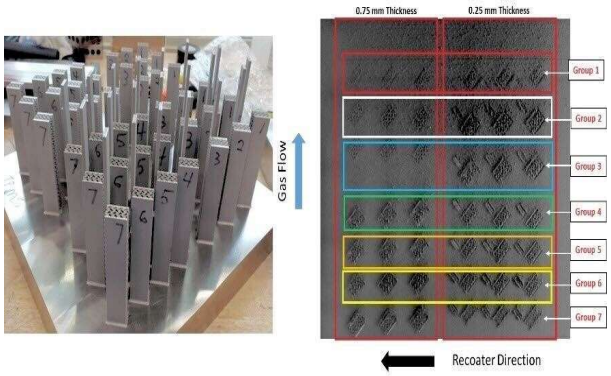

Figure 1. LPBF build plate with different fabricated sample groups of TPMS gyroids of 0.25 mm and 0.75mm

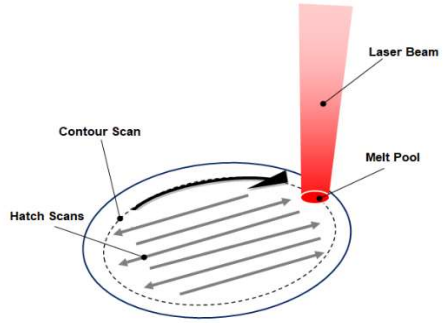

Figure 2. Laser scanning strategies: Contour vs Hatch.

0.25 mm	Contour only	Nominal Speed	C_Nom_0.25
		15% Higher Speed	C+15Nom_0.25
		15% Lower Speed	C-15Nom_0.25
	Hatch only	Nominal Speed	H_Nom_0.25
		15% Higher Speed	H+15Nom_0.25
		15% Lower Speed	H-15Nom_0.25
	Control Sample		Control_0.25
0.75 mm	Contour only	Nominal Speed	C_Nom_0.75
		15% Higher Speed	C+15Nom_0.75
		15% Lower Speed	C-15Nom_0.75
	Hatch only	Nominal Speed	H_Nom_0.75
		15% Higher Speed	H+15Nom_0.75
		15% Lower Speed	H-15Nom_0.75
	Control Sample		Control_0.75

Table 1. Experimental parameter space, where nominal speed is 1250 mm/s.

was commercially available biocompatible Ti-6Al-4V ELI (Grade 23) spherical powder within the size range of 15–45µm (composition: Ti - balance, Al - 6.0, V - 4.0, C - 0.03, Fe - 0.1, O - 0.1, N - 0.01, 3D Systems Inc., USA). The effective spot size, determined by the implemented laser process parameters and powder size distribution, is approximately 100µm. Following the layer-by-layer metal additive manufacturing process, the specimens were separated from the substrate using non-contact wire electric discharge machining (Wire-EDM).

Laser power (W)	Scan speed (mm/s)	Layer thickness (µm)	Beam diam at focus (µm)	Hatch type	Hatch distance (µm)
245	1250	60	60	Strip	82

Table 2. L-PBF process parameters for control sample Ti-6Al-4V ELI (Grade 23)

2.2. Morphological analysis

Micro computed tomography (micro-CT) was performed on the representative witness coupons of 100mm x 10mm x 100 mm across the seven groups to evaluate the morphological parameters of the as-built parts in a General Electric Pheonix V|tome|xL 300 micro/nanoCT system. The 300-kV microfocus tube was used exclusively for imaging of these scans as the smaller 180-kV nanofocus tube did not supply sufficient power to achieve good X-ray transmission. For each sample, 1700 images were acquired on a 2024x2024 detector grid at a voltage of 210kV and 50uA current. Setting detector distance and sample position yielded a voxel size of 10um. Reconstruction of raw image stacks was completed using Volume Graphics (VG2022). Images were reconstructed as 32-bit volume files. (Figure 6) For each specimen, reconstructed 32-bit images with the dimensional information were used as an input in the Avizo software (version 2021.2, Amira-Avizo, FEI, Thermo Fisher Scientific, USA). Binarization of the specimen image was done by thresholding which divided the part into void/pore space and solid material. Pore morphology analysis including the volume percentage of porosity and pore size distribution were calculated using Avizo from the binary images.

2.3. Surface characterization

To evaluate the surface roughness of the as built specimens, Mitutoyo Surface Tester 178-561-12A was used with a stylus tip radius of 2µm. The surface roughness tester was calibrated initially by determining the Ra value for a reference precision calibration specimen. Subsequently, a random tensile sample was selected from each study group, and surface roughness measurements were conducted on five different regions of each sample. The evaluations encompassed assessing the Ra (roughness average), Rz (average maximum height of the profile), and Rq (root mean square roughness) of each surface. The rationale for investigating surface roughness is to correlate mechanical performance with surface topology of interest to applications such as orthopaedic implants where anatomy-specific sites require tailored surface roughness.

2.4. Mechanical characterization

2.4.1. Digital image correlation (DIC)

Digital image correlation (DIC) was employed with an aim to quantify full-field strains on the surface of the study specimens during quasi-static tensile and three-point bending tests. The DIC images were captured using a Flea3 digital camera (FLIR Systems, Inc., USA) with an 8.8 MP resolution at a frequency of 0.5 Hz. The post-processing involving the computational % strain analysis on the recorded images was performed on the commercial software Vic-3D software (Version 7, Correlated Solutions, Inc., USA). The sample preparation for DIC involved generating black speckle patterns through first spray-painting the specimens with white paint, then following a 10-minute drying period. A pressure-controlled airbrush was used to apply random black speckles onto the imaging surface of the specimens.

2.4.2. Quasi-static tensile testing

A total of three samples per study group were subjected to quasi-static tensile test on 30 kN load frames (MTS Inc., USA). According to the ASTM E8 standard [20], displacement control was applied at a displacement rate of 2 mm/s during the tensile testing. The test was carried out until the samples experienced failure. Stress-strain curves were computed from load frame load-displacement data. For every test specimen, the elastic modulus (E), yield stress (σ_y), ultimate tensile strength (S_{UT}) was calculated from the stress-strain curves. Elastic modulus was determined as the slope of the linear elastic region, and the yield stress was calculated using the 0.2% offset of the elastic modulus line.

2.4.3. Flexural strength characterization

The three-point bending tests were conducted on 2 samples per study group of both 0.25 mm and 0.75 mm sheet thicknesses using load frames equipped with bending fixtures and a static load limit of 30 kN. A displacement control rate of 0.008 mm/s was implemented, following the guidelines of ASTM E290 [36]. Testing concluded upon specimen fracture or the observation of a sudden drop in the applied load. From the bending plots, maximum flexural stiffness was calculated which is the ratio of maximum load to the maximum deformation.

2.5. Statistical analysis

The statistical analysis was performed using the Minitab Statistical Software Version 21.1.0 (2023 Minitab, LLC.) Statistical significance was assessed using one-way ANOVA, followed by Tukey's test for conducting pairwise comparisons among the various study groups.

3. Results

3.1. Surface characteristics of as-built Samples

Surface characterization was performed to assess the surface roughness, employing three key parameters: Ra, Rz, and Rq. The investigation yielded noteworthy insights consistently across all the 3 processing conditions (Figure 3, Figure 4, and Figure 5). The control sample was observed to have the lowest surface roughness (Ra-7.56 µm) among all examined samples, indicating a baseline for minimal irregularities on the surface. In the case of the hatch strategy, any deviation from nominal scan speed corresponded to an increase in surface roughness. This observation suggests a sensitivity of surface roughness to changes in the scan speed for the hatch strategy, emphasizing the need for careful consideration when implementing variations in this parameter. Conversely, for the contour strategy, deviations in scan speed from its nominal value resulted in a reduction in surface roughness. This trend indicates a contrasting effect compared to the hatch strategy.

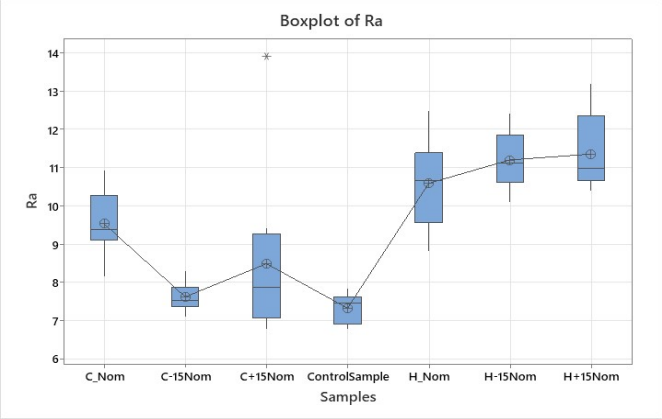

Figure 3. Boxplot of Ra for the different sample groups

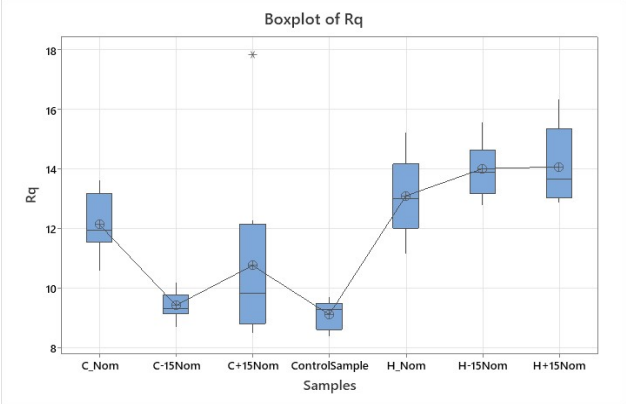

Figure 4. Boxplot of Rq for the different sample groups.

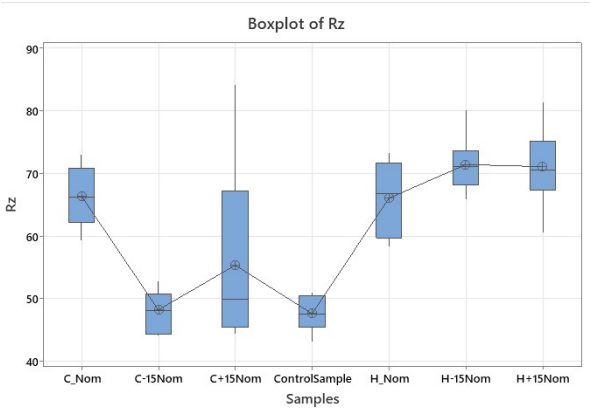

Figure 5. Boxplot of Rz for the different sample groups.

3.2. Morphological properties

Micro-CT analysis was conducted to compute the density (%) of different sample groups. According to the findings shown in Figure 6, the sample group "Contour Only Nominal Speed" exhibited a slightly lower density compared to all the other samples. These results imply minor variations in relative density values among the remaining groups, except for the "C_Nom" sample group. The overall trend suggests a similarity in density across most of the samples, indicating that the employed contour and hatch scan strategies, along with their respective variations in scan speed, do not lead to substantial differences in relative density.

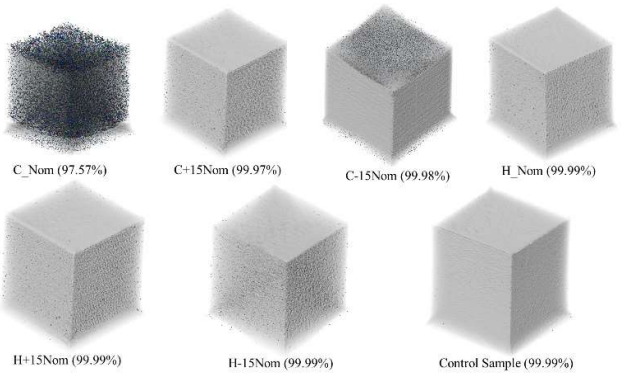

Figure 6. Relative densities (%) of different sample groups.

3.3. Quasi-static tensile responses

Quasi-static tensile responses were collected from various dog bone samples subjected to different Ti6Al4V AM scan processing conditions, as detailed in Table 3. The stress-strain curves derived from static tensile tests facilitated the determination of ultimate tensile strength (UTS) and elongation (%). As shown in Figure 7, Sample 2 (C+15Nom) showed the highest UTS of 1194.9867 MPa, while the Sample C_Nom showed the lowest UTS of 60.14 MPa. Samples C+15Nom, C-15Nom, H_Nom, H+15Nom, and H-15Nom exhibited UTS values ranging closely around 1133 to 1194 MPa, suggesting consistent performance and stability despite variations in scan speed and scan strategies. Similarly, the control sample lies closely within this consistent trend with a UTS of 1175.833 MPa. The analysis of variance (ANOVA) yielded a significant p-value of 0.0005, indicating differences among the sample groups. However, employing the Tukey method of comparison with a 95% confidence level (Table 4) reveals that Sample 1 (C_Nom) is significantly different from all other sample groups. In contrast, the remaining six sample groups share the same letter group, signifying that they are not statistically different from each other in terms of ultimate tensile strength. This emphasizes the general homogeneity of UTS among all the sample groups except C_Nom.

Sample	Ultimate Tensile Strengths (Sut) (MPa)	Elongation (%)	Elastic Modulus (MPa)
C_Nom	60.14 ± 18	-	3172 ± 320.22
C+15Nom	1194.98 ± 18.55	20.27 ± 0.66	8518.73 ± 629.75
C-15Nom	1133.74 ± 47.35	19.57 ± 2.45	9438.62 ± 229.04
H_Nom	1154.90 ± 43.22	18.37 ± 2.64	9525.42 ± 241.35
H+15Nom	1137.46 ± 43.18	17.37 ± 1.46	9517.29 ± 95.32
H-15Nom	1192.97 ± 41.82	17.48 ± 1.45	9672.67 ± 339.84
LT60	1175.83 ± 54.74	20.81 ± 2.45	9553.3 ± 36.86

Table 3. Summary of the mechanical tensile properties.

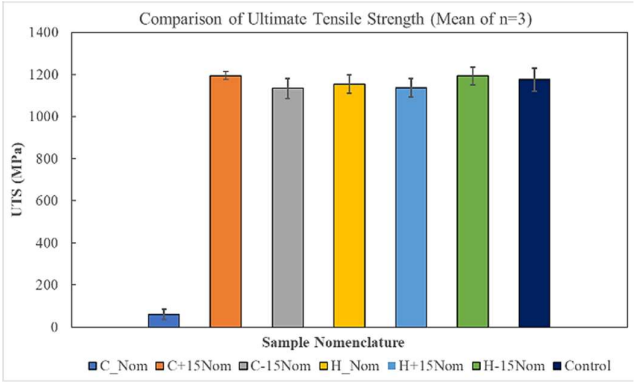

Figure 7. Comparison of Ultimate Tensile Strengths.

Nomenclature	N	Mean	Grouping
C+15Nom	3	1195.0	A
H-15Nom	3	1193.0	A
LT60	3	1175.8	A
H_Nom	3	1154.9	A
H+15Nom	3	1137.5	A
C-15Nom	3	1133.7	A
C_Nom	3	60.14	B

Means that do not share a letter are significantly different.

Table 4. Tukey UTS mean- comparison of sample groups.

The % elongation was also compared for all the sample groups (Table 3) except the contour nominal speed (C_Nom), reason being it has the lowest strain under tension, and hence was excluded from the tensile elongation analysis due to its minimal elongation behavior. From the comparison (Figure 8), the control sample exhibited the highest tensile elongation (20.81%), indicating superior deformability before reaching fracture. The ANOVA yielded a p value of 0.232 (p value > 0.05) indicating no significant differences between all the sample groups. This conclusion is consistent with the Tukey method of comparison of the group means with a 95% confidence level. (Table 5).

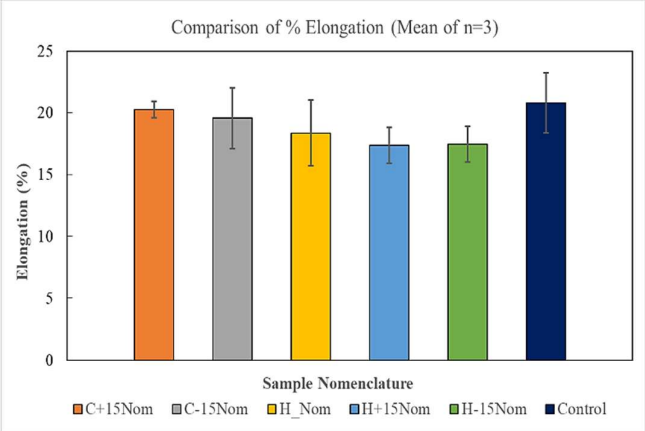

Figure 8. Comparison of % Elongation.

Nomenclature	N	Mean	Grouping
LT60	3	20.81	A
C+15Nom	3	20.273	A
C-15Nom	3	19.57	A
H_Nom	3	18.37	A
H-15Nom	3	17.483	A
H+15Nom	3	17.367	A

Means that do not share a letter are significantly different.

Table 5. Tukey % elongation comparison of sample groups.

The outcomes obtained from Digital Image Correlation (DIC) tensile test analysis revealed a consistent trend in the percentage strain across all sample groups. Notably, the observed percentage strain closely follows the same trend as for the calculated percentage elongation for each of the sample groups.

In addition, the elastic modulus was also calculated and compared for the different sample groups. From the comparison in Figure 9, the sample group C_Nom showed the lowest elastic modulus of 3172 MPa, and the sample group C+15 Nom showed an elastic modulus of 8518.73 MPa. All the other sample groups exhibited Elastic modulus values ranging closely from around 9438.62 to 9672.67 MPa. The Tukey method of comparison with a 95% confidence level (Table 6) reveals that Sample 1 (C_Nom) and Sample group 2 (C+15Nom) are significantly different from all other sample groups and share different letter groups. In contrast, the remaining six sample groups share the same letter group, signifying that they are not statistically different from each other in terms of elastic modulus.

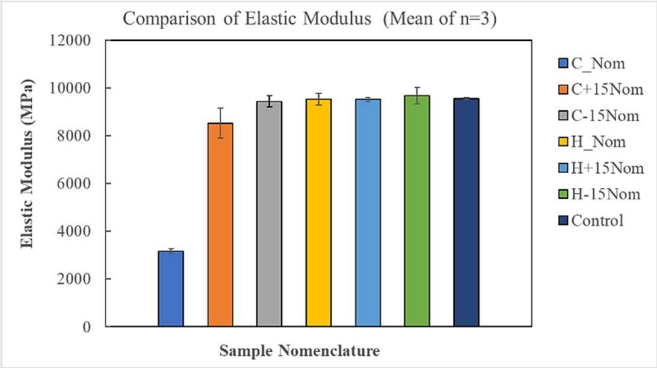

Figure 9. Comparison of Elastic Modulus.

Nomenclature	N	Mean	Grouping
H-15Nom	3	9673	A
LT60	3	9553.3	A
H_Nom	3	9525	A
H+15Nom	3	9517.3	A
C-15Nom	3	9439	A
C+15Nom	3	8519	B
CNom	3	3173	C

Means that do not share a letter are significantly different.

Table 6. Tukey Elastic modulus comparison of sample groups.

3.4. Flexural behavior

Quasi-static three-point bending responses for TPMS gyroid of 0.25 and 0.75mm sheet thickness are presented in Figure 11 and Figure 12. Based on Figure 11, force-displacement curves for the 0.25 mm TPMS gyroid structures, it was observed that the sample subjected to the contour-only nominal speed exhibited the lowest deformation behavior. In contrast, all other samples displayed an increasing trend of deformation behavior, surpassing that of the control sample. On the other hand, for the 0.75mm sheet thickness TPMS gyroid structures (Figure 12), it was observed that the deformation behavior was almost similar for all the sample groups, except for the contour only nominal speed scan strategy.

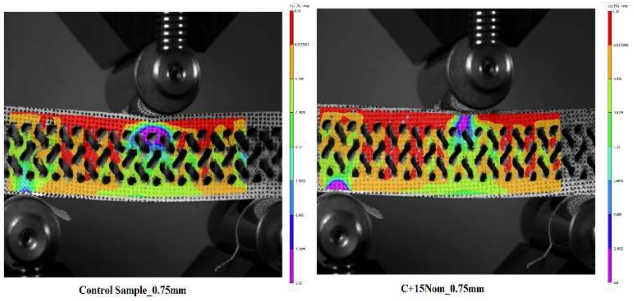

Figure 10. DIC strain data for control sample and C+15Nom for 0.75mm gyroid sheet thickness lattices.

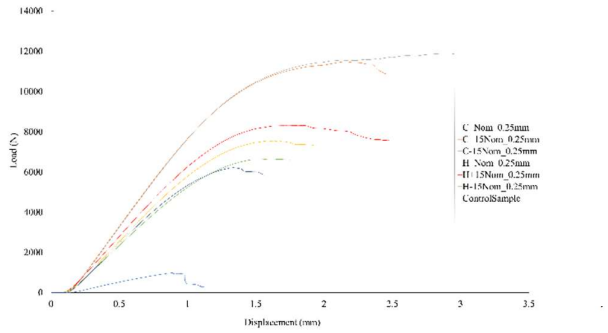

Figure 11. Average Load vs Deformation curves 0.25 mm sheet thickness TPMS lattices.

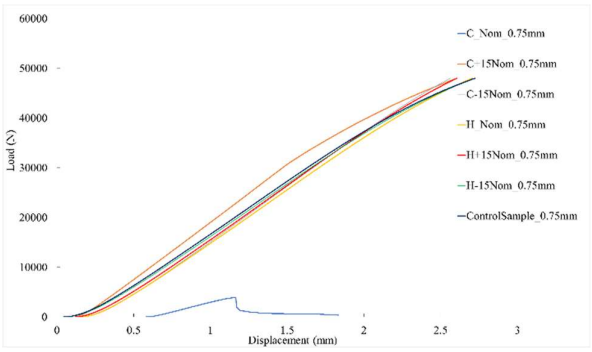

Figure 12. Average Load vs Deformation curves 0.75 mm sheet thickness TPMS lattices.

An increasing trend in flexural stiffness for both sheet thickness was observed as seen in Figure 13 across all the sample variations from the control sample, except the C_Nom. Also, as expected the flexural stiffness of 0.75 mm sheet thickness is seen to be higher than 0.25mm sheet thickness

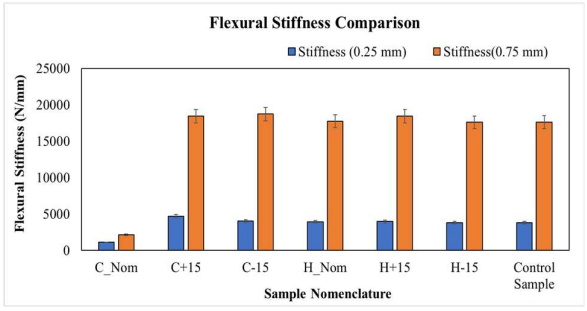

Figure 13. Comparison of maximum flexural stiffness for 0.25 mm and 0.75 sheet thickness TPMS lattices.

lattice structure.

4. Discussion

4.1. Tensile Testing

Interestingly, similar mechanical properties, specifically Ultimate Tensile Strength (UTS), elastic modulus, and % elongation were observed, except for the contour only with nominal scan speed (C_Nom) strategy which stands different. Most variations, including different scan strategies and varied speeds, did not induce significant deviations in UTS and elastic modulus. This suggests that the mechanical properties of the manufactured components remain largely unaffected by alterations in the scanning parameters. The UTS of Ti6Al4V manufactured by LPBF AM with different scan speed and strategy variations and constant laser power of 245W found in this paper is consistent with the literature. ([23], [24], [25], [26])

4.2. Surface roughness

In general, deviations from the control sample in terms of scan speed and strategy tend to result in an increase in surface roughness. This observation aligns with expectations, as variations in scan speed and strategy are anticipated to generate a relatively less stable and controlled melt pool at the surface. The consequence of this less controlled process manifests as more irregular surface roughness, contributing to the observed increase. ([27], [28], [29])

4.3. Micro- CT

The micro-CT results for LPBF additively manufactured Ti6Al4V have revealed consistently excellent density across various parameters. Interestingly, a key insight emerges from this analysis: within a range of ±15% from the nominal speed, no deviation from nominal density is expected. It is important to note that the laser power should be constant. This observation holds significant implications as it can be treated as a concurrent design and processing variable in LPBF additive manufacturing process using Ti6Al4V alloy. Carrozza et al. [37] conducted a study where they printed multiple thin-walled Ti6Al4V structures using Laser Powder Bed Fusion (LPBF). They observed a correlation between the width of the specimens and their porosity, microstructure, and hardness. Despite lower wall thickness (300 µm) and channel diameter (1 mm), Ti6Al4V alloy demonstrated good processability, with observed relative density values ranging from 97% to 99%. Also, Wu et al. [38] suggested that higher porosity levels could be expected in thin Ti6Al4V structures due to the unpredictable melt pool shape in this context, potentially leading to increased process-related defects. Based on the literature, it is anticipated that higher levels of porosity will be observed in structures with a 0.25 mm sheet thickness compared to those with a 0.75 mm thickness, even under optimal process parameters. Consequently, the authors plan to conduct further examinations of the morphological properties, using micro-CT imaging, on thin sheet TPMS, and include microstructure characterization in future studies.

4.4. Flexural Behavior

To the best of authors' knowledge, this study is the first to report on the flexural behavior of the different lattice sheet thickness with varying process scan strategy and speed conditions. The gyroid's flexural stiffness proportionally varies between 0.25 mm and 0.75 mm thicknesses, as anticipated. Moreover, scan parameter deviations impact flexural stiffness, generally resulting in increased stiffness from the control sample. This increase in stiffness implies a transition toward less ductile material response. A substantial rise in flexural stiffness, ranging from 48% to 79%, was noted in the 0.75 mm sheet thickness lattice in comparison to the 0.25 mm sheet thickness lattice. This significant increase underscores the considerable impact of sheet thickness on flexural stiffness, suggesting a notable difference in structural rigidity between the two thickness variants. The results from DIC (Figure 10) show an agreement in strain-maps for all samples of the same sheet thickness (with the exception of sample C_Nom for both study groups). A comparative visualization between two sample groups (the 0.75mm thick control and sample C+15Nom) are shown for a visual comparison of strain distribution during testing at a displacement of 0.125 mm and a force of 328.6 N.

5. Conclusion

This study comprehensively explored the manufacturing of Triply Periodic Minimal Surface (TPMS) lattices using Laser-Powder Bed Fusion (LPBF) and investigated the influence of laser scan parameters on mechanical properties. Notably, consistent mechanical tensile properties were achieved across various scan strategies and speeds, except for the contour-only nominal speed (C_Nom) strategy. Surface roughness exhibited an expected increase with deviations from the control sample, aligning with the anticipated influence of scan speed and strategy on melt pool stability. Micro-CT results for Ti6Al4V showcased excellent density, emphasizing a valuable design rule: within a ±15% range from the nominal speed, maintaining constant power, no deviation from this excellent density was expected. Unprecedented insights into the flexural behavior of TPMS lattices, particularly the significant increase in stiffness with 0.75 mm thickness compared to 0.25 mm, were uncovered. This suggested the potential for functional grading of lattice designs by varying laser scanning strategies. These findings provided a crucial foundation for achieving uniform mechanical properties and functionally graded density in lattice structures, unlocking new possibilities for diverse applications.

Acknowledgements

We would like to thank, Sagar Jalui for providing insights on surface characterization, Yasham Mundada for reviewing the manuscript, Ryan Overdorff for fabrication and machining expertise and Center of Quantitative Imaging, Penn State University for their assistance in micro-CT. Part of this work was supported by NSF CMMI award#2130694.

References

[1] Tilton, M., Borjali, A., Griffis, J. C., Varadarajan, K. M., & Manogharan, G. P. (2023). Fatigue properties of Ti-6Al-4V TPMS scaffolds fabricated via laser powder bed fusion. Manufacturing Letters, 37, 32–38. https://doi.org/10.1016/j.mfglet.2023.06.005

[2] Tilton, M., Borjali, A., Isaacson, A., Varadarajan, K. M., & Manogharan, G. P. (2021). On structure and mechanics of biomimetic meta-biomaterials fabricated via metal additive manufacturing. Materials & Design, 201, 109498. https://doi.org/10.1016/j.matdes.2021.109498

[3] Tilton, M., Jacobs, E., Overdorff, R., Astudillo Potes, M., Lu, L., & Manogharan, G. (2023). Biomechanical behavior of PMMA 3D printed biomimetic scaffolds: Effects of physiologically relevant environment. Journal of the Mechanical Behavior of Biomedical Materials, 138, 105612. https://doi.org/10.1016/j.jmbbm.2022.105612

[4] Jones, A., Leary, M., Bateman, S., & Easton, M. (2021). Effect of surface geometry on laser powder bed fusion defects. Journal of Materials Processing Technology, 296, 117179. https://doi.org/10.1016/j.jmatprotec.2021.117179

[5] Zhang, L., Feih, S., Daynes, S., Chang, S., Wang, M. Y., Wei, J., & Lu, W. F. (2018). Energy absorption characteristics of metallic triply periodic minimal surface sheet structures under compressive loading. Additive Manufacturing, 23, 505–515. https://doi.org/10.1016/j.addma.2018.08.007

[6] Al-Ketan, O., Rowshan, R., & Abu Al-Rub, R. K. (2018). Topology-mechanical property relationship of 3D printed strut, skeletal, and sheet based periodic metallic cellular materials. Additive Manufacturing, 19, 167–183. https://doi.org/10.1016/j.addma.2017.12.006

[7] A. M. Abou-Ali, O. Al-Ketan, D.-W. Lee, R. Rowshan, and R. K. Abu Al-Rub, "Mechanical behavior of polymeric selective laser sintered ligament and sheet-based lattices of triply periodic minimal surface architectures," *Mater Des*, vol. 196, p. 109100, Nov. 2020, doi: 10.1016/j.matdes.2020.109100.

[8] M. Ouda *et al.*, "Novel static mixers based on triply periodic minimal surface (TPMS) architectures," *J Environ Chem Eng*, vol. 8, no. 5, p. 104289, Oct. 2020, doi: 10.1016/j.jece.2020.104289.

[9] O. Elliott *et al.*, "Design and Manufacturing of High Surface Area 3D-Printed Media for Moving Bed Bioreactors for Wastewater Treatment," *J Contemp Water Res Educ*, vol. 160, no. 1, pp. 144–156, Apr. 2017, doi: 10.1111/j.1936-704X.2017.03246. x.

[10] O. Al-Ketan, M. Pelanconi, A. Ortona, and R. K. Abu Al-Rub, "Additive manufacturing of architected catalytic ceramic substrates based on triply periodic minimal surfaces," *Journal of the American Ceramic Society*, vol. 102, no. 10, pp. 6176–6193, Oct. 2019, doi: 10.1111/jace.16474.

[11] J. G. Werner, S. S. Johnson, V. Vijay, and U. Wiesner, "Carbon–Sulfur Composites from Cylindrical and Gyroidal Mesoporous Carbons with Tunable Properties in Lithium–Sulfur Batteries," *Chemistry of Materials*, vol. 27, no. 9, pp. 3349–3357, May 2015, doi: 10.1021/acs.chemmater.5b00500.

[12] T. Femmer, A. J. C. Kuehne, and M. Wessling, "Estimation of the structure dependent performance of 3-D rapid prototyped membranes," *Chemical Engineering Journal*, vol. 273, pp. 438–445, Aug. 2015, doi: 10.1016/j.cej.2015.03.029.

[13] X. Guo *et al.*, "Interpenetrating phase composites with 3D printed triply periodic minimal surface (TPMS) lattice structures," *Compos B Eng*, vol. 248, p. 110351, Jan. 2023, doi: 10.1016/j.compositesb.2022.110351.

[14] S. RAJAGOPALAN and R. ROBB, "Schwarz meets Schwann: Design and fabrication of biomorphic and durataxic tissue engineering scaffolds," *Med Image Anal*, vol. 10, no. 5, pp. 693–712, Oct. 2006, doi: 10.1016/j.media.2006.06.001.

[15] C. Lin, G. Wen, H. Yin, Z.-P. Wang, J. Liu, and Y. M. Xie, "Revealing the sound insulation capacities of TPMS sandwich panels," *J Sound Vib*, vol. 540, p. 117303, Dec. 2022, doi: 10.1016/j.jsv.2022.117303.

[16] L. Elomaa, S. Teixeira, R. Hakala, H. Korhonen, D. W. Grijpma, and J. V. Seppälä, "Preparation of poly(ε-caprolactone)-based tissue engineering scaffolds by stereolithography," *Acta Biomater*, vol. 7, no. 11, pp. 3850–3856, Nov. 2011, doi: 10.1016/j.actbio.2011.06.039.

[17] L. Zhang *et al.*, "Pseudo-ductile fracture of 3D printed alumina triply periodic minimal surface structures," *J Eur Ceram Soc*, vol. 40, no.

2, pp. 408–416, Feb. 2020, doi: 10.1016/j.jeurceramsoc.2019.09.048.

[18] H. Fu, X. Huang, and S. Kaewunruen, "Experimental investigations into nonlinear dynamic behaviours of triply periodical minimal surface structures," *Compos Struct*, vol. 323, p. 117510, Nov. 2023, doi: 10.1016/j.compstruct.2023.117510.

[19] N. Wang, G. K. Meenashisundaram, S. Chang, J. Y. H. Fuh, S. T. Dheen, and A. Senthil Kumar, "A comparative investigation on the mechanical properties and cytotoxicity of Cubic, Octet, and TPMS gyroid structures fabricated by selective laser melting of stainless steel 316L," *J Mech Behav Biomed Mater*, vol. 129, p. 105151, May 2022, doi: 10.1016/j.jmbbm.2022.105151.

[20] Mechanical testing of metals Ductility testing. (2022). ISO 13314:2011.

[21] S. Catchpole-Smith, R. R. J. Sélo, A. W. Davis, I. A. Ashcroft, C. J. Tuck, and A. Clare, "Thermal conductivity of TPMS lattice structures manufactured via laser powder bed fusion," *Addit Manuf*, vol. 30, p. 100846, Dec. 2019, doi: 10.1016/j.addma.2019.100846.

[22] M. Tilton, A. Borjali, J. C. Griffis, K. M. Varadarajan, and G. P. Manogharan, "Fatigue properties of Ti-6Al-4V TPMS scaffolds fabricated via laser powder bed fusion," *Manuf Lett*, vol. 37, pp. 32–38, Sep. 2023, doi: 10.1016/j.mfglet.2023.06.005.

[23] J. P. Kelly *et al.*, "Binder jet additive manufacturing of ceramic heat exchangers for concentrating solar power applications with thermal energy storage in molten chlorides," *Addit Manuf*, vol. 56, p. 102937, Aug. 2022, doi: 10.1016/j.addma.2022.102937.

[24] V. Sufiiarov, A. Kantyukov, A. Popovich, and A. Sotov, "Synthesis of Spherical Powder of Lead-Free BCZT Piezoceramics and Binder Jetting Additive Manufacturing of Triply Periodic Minimum Surface Lattice Structures," *Materials*, vol. 15, no. 18, p. 6289, Sep. 2022, doi: 10.3390/ma15186289.

[25] M. Pelanconi *et al.*, "New, 3D binder-jetted carbons with minimal periodic surface structures," *Carbon N Y*, vol. 213, p. 118252, Sep. 2023, doi: 10.1016/j.carbon.2023.118252.

[26] M. Kurup and J. Pitchaimani, "Aeroelastic flutter of triply periodic minimal surface (TPMS) beams," *Composites Part C: Open Access*, vol. 10, p. 100349, Mar. 2023, doi: 10.1016/j.jcomc.2023.100349.

[27] J. Liu, G. Li, Q. Sun, H. Li, J. Sun, and X. Wang, "Understanding the effect of scanning strategies on the microstructure and crystallographic texture of Ti-6Al-4V alloy manufactured by laser powder bed fusion," *J Mater Process Technol*, vol. 299, p. 117366, Jan. 2022, doi: 10.1016/j.jmatprotec.2021.117366.

[28] Q. Yan *et al.*, "Comparison study on microstructure and mechanical properties of Ti-6Al-4V alloys fabricated by powder-based selective-laser-melting and sintering methods," *Mater Charact*, vol. 164, p. 110358, Jun. 2020, doi: 10.1016/j.matchar.2020.110358.

[29] Ż. A. Mierzejewska, R. Hudák, and J. Sidun, "Mechanical Properties and Microstructure of DMLS Ti6Al4V Alloy Dedicated to Biomedical Applications," *Materials*, vol. 12, no. 1, p. 176, Jan. 2019, doi: 10.3390/ma12010176.

[30] Z. Wang, Z. Xiao, Y. Tse, C. Huang, and W. Zhang, "Optimization of processing parameters and establishment of a relationship between microstructure and mechanical properties of SLM titanium alloy," *Opt Laser Technol*, vol. 112, pp. 159–167, Apr. 2019, doi: 10.1016/j.optlastec.2018.11.014.

[31] D. Wang, J. Lv, X. Wei, D. Lu, and C. Chen, "Study on Surface Roughness Improvement of Selective Laser Melted Ti6Al4V Alloy," *Crystals (Basel)*, vol. 13, no. 2, p. 306, Feb. 2023, doi: 10.3390/cryst13020306.

[32] Z. Chen, X. Wu, D. Tomus, and C. H. J. Davies, "Surface roughness of Selective Laser Melted Ti-6Al-4V alloy components," *Addit Manuf*, vol. 21, pp. 91–103, May 2018, doi: 10.1016/j.addma.2018.02.009.

[33] D. Simson and S. K. Subbu, "Effect of Process Parameters on Surface Integrity of LPBF Ti6Al4V," *Procedia CIRP*, vol. 108, pp. 716–721, 2022, doi: 10.1016/j.procir.2022.03.111.

[34] Qu, S., Ding, J., & Song, X. (2021). Achieving Triply Periodic Minimal Surface Thin-Walled Structures by Micro Laser Powder Bed Fusion Process. Micromachines, 12(6), 705. https://doi.org/10.3390/mi12060705

[35] Hussain, S., Alagha, A. N., & Zaki, W. (2024). Phase Transformation Behavior of NiTi Triply Periodic Minimal Surface Lattices Fabricated by Laser Powder Bed Fusion. Journal of Materials Engineering and Performance. https://doi.org/10.1007/s11665-024-09162-7

[36] Standard Test Methods for Bend Testing of Material for Ductility. (ASTM 290).

[37] Carrozza, A., Bircher, B. A., Aversa, A., & Biamino, S. (2023). Investigating Complex Geometrical Features in LPBF-Produced Parts: A Material-Based Comparison Between Different Titanium Alloys. Metals and Materials International, 29(12), 3697–3714. https://doi.org/10.1007/s12540-023-01460-4

[38] Wu, Z., Narra, S. P., & Rollett, A. (2020). Exploring the fabrication limits of thin-wall structures in a laser powder bed fusion process. The International Journal of Advanced Manufacturing Technology, 110(1–2), 191–207. https://doi.org/10.1007/s00170-020-05827-4

.